

Origin of vibrational wavepacket dynamics in Fe carbene photosensitizer determined with femtosecond X-ray emission and scattering

Kristjan Kunnus¹, Morgane Vacher², Tobias C. B. Harlang^{3,4}, Kasper S. Kjær^{1,3,4}, Kristoffer Haldrup⁴, Elisa Biasin^{1,4}, Tim B. van Driel⁵, Mátyás Pápai⁶, Pavel Chabera³, Yizhu Liu^{3,7}, Hideyuki Tatsuno³, Cornelia Timm³, Erik Källman², Mickaël Delcey², Robert W. Hartsock¹, Marco E. Reinhard¹, Sergey Koroidov¹, Mads G. Laursen⁴, Frederik B. Hansen⁴, Peter Vester⁴, Morten Christensen⁴, Lise Sandberg^{4,13}, Zoltán Németh⁸, Dorottya Sárosiné Szemes⁸, Éva Bajnóczi⁸, Roberto Alonso-Mori⁵, James M. Glowia⁵, Silke Nelson⁵, Marcin Sikorski⁵, Dimosthenis Sokaras⁹, Henrik T. Lemke⁵, Sophie Canton^{10,11}, Klaus B. Møller⁶, Martin M. Nielsen⁴, György Vankó⁸, Kenneth Wärnmark⁷, Villy Sundström³, Petter Persson¹², Marcus Lundberg², Jens Uhlig³, Kelly J. Gaffney¹

Affiliations

¹ PULSE Institute, SLAC National Accelerator Laboratory, Stanford University, Menlo Park, California 94025, United States.

² Department of Chemistry - Ångström laboratory, Uppsala University, Box 538, 75121 Uppsala, Sweden

³ Department of Chemical Physics, Lund University, P.O. Box 124, 22100 Lund, Sweden

⁴ Department of Physics, Technical University of Denmark, DK-2800, Lyngby, Denmark.

⁵ LCLS, SLAC National Accelerator Laboratory, Menlo Park, California 94025, United States.

⁶ Department of Chemistry, Technical University of Denmark, Kemitorvet 207, DK-2800 Kongens Lyngby, Denmark

⁷ Centre for Analysis and Synthesis, Department of Chemistry, Lund University, P.O. Box 124, 22100 Lund, Sweden

⁸ Wigner Research Centre for Physics, Hungarian Academy of Sciences, P.O. Box 49, H-1525 Budapest, Hungary

⁹ SSRL, SLAC National Accelerator Laboratory, Menlo Park, California 94025, United States.

¹⁰ ELI-ALPS, ELI-HU Non-Profit Ltd., Dugonics ter 13, Szeged 6720, Hungary

¹¹ FS-ATTO, Deutsches Elektronen-Synchrotron (DESY), Notkestrasse 85, D-22607 Hamburg, Germany

¹² Theoretical Chemistry Division, Lund University, P.O. Box 124, 22100 Lund, Sweden

¹³ University of Copenhagen, Niels Bohr Institute, Blegdamsvej 17, 2100 Copenhagen, Denmark

Abstract

Disentangling the dynamics of electrons and nuclei during nonadiabatic molecular transformations remains a considerable experimental challenge. Here we have investigated photoinduced electron transfer dynamics following a metal-to-ligand charge-transfer (MLCT) excitation of the $[\text{Fe}(\text{bmip})_2]^{2+}$ photosensitizer, where $\text{bmip} = 2,6\text{-bis}(3\text{-methyl-imidazole-1-ylidene})\text{-pyridine}$, with simultaneous femtosecond-resolution Fe $K\alpha$ and $K\beta$ X-ray Emission Spectroscopy (XES) and Wide Angle X-ray Scattering (WAXS). This measurement clearly shows temporal oscillations in the XES and WAXS difference signals with the same 278 fs period oscillation. The oscillatory signal originates from an Fe-ligand stretching mode vibrational wavepacket on a triplet metal-centered (^3MC) excited state surface. The vibrational wavepacket is created by 40% of the excited population that undergoes electron transfer from the non-equilibrium MLCT excited state to the ^3MC excited state with a 110 fs time constant, while the other 60% relaxes to a $^3\text{MLCT}$ excited state in parallel. The sensitivity of the $K\alpha$ XES spectrum to molecular structure results from core-level vibronic coupling, due to a 0.7% average Fe-ligand bond length difference in the lowest energy geometry of the 1s and 2p core-ionized states. These results highlight the importance of vibronic effects in time-resolved XES experiments and demonstrate the role of metal-centered excited states in the electronic excited state relaxation dynamics of an Fe carbene photosensitizer.

Mechanistic understanding of ultrafast nonadiabatic photo-physical and photo-chemical processes requires correlating the coupled dynamics of the many electronic and nuclear degrees of freedom [1,2]. Deeper knowledge of molecular-level dynamics has the potential to inform the development of efficient and cost-effective functional materials. In particular, progress in the synthesis of novel Fe-based molecular photosensitizers [3,4] highlights a continuing need for a better understanding of intramolecular photoinduced electronic excited state processes in these systems [5–7]. A central challenge to developing Fe-based molecular photosensitizers and photocatalysts is controlling the interplay between charge transfer (CT) and metal centered (MC) excited states. Characterizing this interplay has proven difficult for ultrafast optical methods because of the lack of clear spectroscopic signatures of MC excited states, and highlights the strengths of ultrafast x-ray spectroscopy and scattering methods [8,9].

A powerful method to disentangle the electronic and nuclear motions of 3d transition metal complexes during ultrafast nonadiabatic processes is time-resolved 1s-2p ($K\alpha$) and 1s-3p ($K\beta$) X-ray Emission Spectroscopy (XES) [10–14] combined with Wide Angle X-ray Scattering (WAXS) [15–23]. These experiments have been utilized to assign the electronic and structural motions during excited state dynamics [24–26] and to project the locations of conical intersections between excited state potential energy surfaces onto critical structural coordinates [27]. Robust tracking of electronic state populations in these studies has relied on the demonstrated sensitivity of the XES spectra to the charge and spin density on the 3d transition metal [28–31] and the presumed insensitivity of $K\alpha/K\beta$ XES to bonding geometry. This approach for interpreting time resolved $K\beta$ XES measurements has been effective for initial time-resolved investigations, but the role of nuclear structure on XES spectra remains unclear.

Coherent nuclear dynamics are ubiquitous in photoexcited systems. Oscillatory wavepacket motions have been clearly measured in time-resolved WAXS [19,27,32], however the effects of purely nuclear dynamics in ultrafast $K\alpha/K\beta$ XES has not been observed [10–14]. This contrasts with other X-ray spectroscopic methods that directly involve valence orbitals, such as X-ray absorption [33–38] and resonant inelastic X-ray scattering [39–41], which are sensitive to both electronic and nuclear structure. The development of ultrafast XES requires understanding the impact of nuclear dynamics on $K\alpha$ and $K\beta$ XES spectra.

This study focuses on the application of ultrafast XES and WAXS to photoinduced electronic excited state dynamics in the Fe carbene complex $[\text{Fe}(\text{bmip})_2]^{2+}$ [bmip = 2,6-bis(3-methylimidazole-1-ylidene)-pyridine] (Fig. 1A) [42–44]. The strong σ -bonding of metal-carbene complexes leads to destabilization of MC excited states and this generates uncharacteristically long $^3\text{MLCT}$ lifetimes for iron complexes [42] and a high electron injection efficiency [45]. These experimental findings have motivated theoretical studies focused on understanding the $^3\text{MLCT}$ excited state relaxation mechanism [46–48]. Unlike the experimental studies, quantum dynamical simulations indicate fast population of the ^3MC excited states in $[\text{Fe}(\text{bmip})_2]^{2+}$, with only 1/3 of the excited state population remaining in the MLCT manifold and 2/3 forming a ^3MC excited state with a ~ 1 ps time constant [47]. Addressing the discrepancies between the interpretation of ultrafast optical spectroscopy and quantum dynamics studies requires robust signatures for MLCT and MC excited states and motivates our time-resolved XES and WAXS study of the coupled electronic and structural dynamics of $[\text{Fe}(\text{bmip})_2]^{2+}$. Contrary to prior ultrafast XES measurements on transition metal complexes [10–14], the $K\alpha$ XES signal of $[\text{Fe}(\text{bmip})_2]^{2+}$ shows the signature of vibrational wavepacket dynamics. We verify the assignment of the oscillations in the $K\alpha$ XES signal with the simultaneous observation of the same wavepacket dynamics with WAXS and assign the oscillations to a Fe-ligand bond stretching coordinate of a ^3MC excited state. Combining these experimental observations with quantum chemical simulations, we quantify the core-level vibronic coupling responsible for the XES structural sensitivity and provide a framework for understanding the origin of vibronic effects in time-resolved XES experiments.

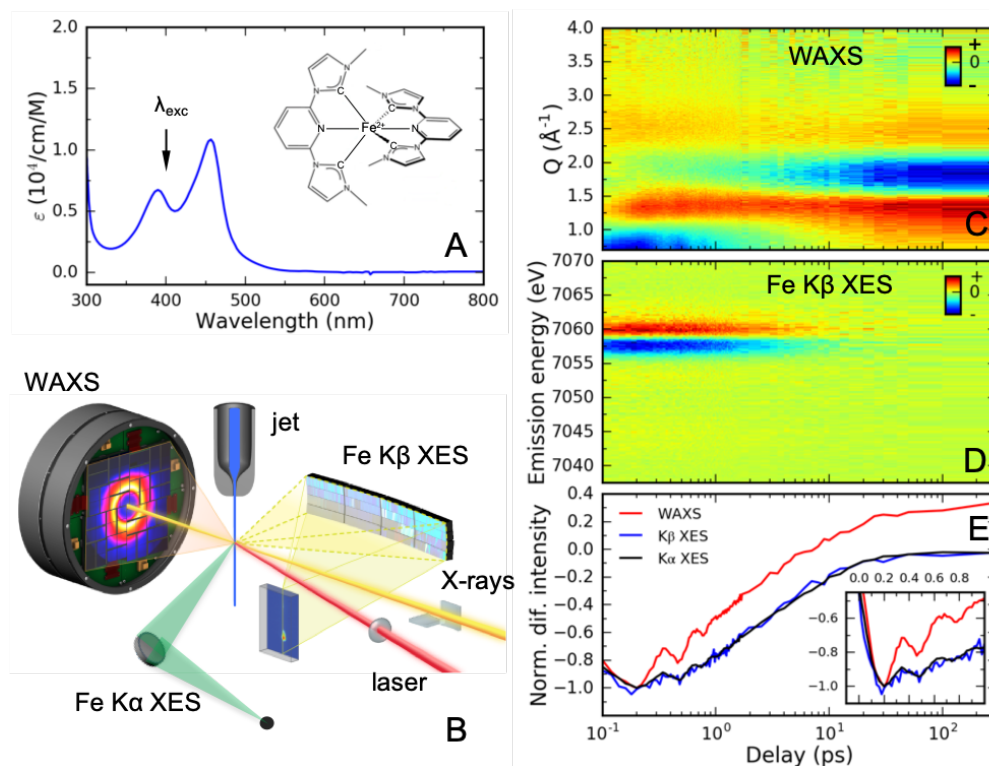


Fig. 1. Simultaneous tracking of femtosecond photoinduced dynamics with X-ray scattering and emission. (A) UV-visible absorption spectrum of $[\text{Fe}(\text{bmip})_2]^{2+}$ in acetonitrile and its chemical structure (inset). (B) Schematic of the experimental setup. Time-resolved difference signals of (C) WAXS (Q – length of the scattering vector), (D) $\text{K}\beta$ X-ray emission and (E) $\text{K}\alpha/\text{K}\beta$ XES and WAXS traces (black: $\text{K}\alpha$ at 6404.3 eV; blue: $\text{K}\beta$ between 7056 – 7058.5 eV; red: WAXS between 0.7 – 1.0 \AA^{-1}). Inset highlights the oscillatory component of XES and WAXS signals. Difference traces normalized to -1 at the minimum ($\text{K}\beta$ scaled to maximize overlap with $\text{K}\alpha$).

Results

We probed the dynamics of $[\text{Fe}(\text{bmip})_2]^{2+}$ dissolved in acetonitrile following 400 nm photoexcitation of a MLCT excited state with ultrafast WAXS and Fe $\text{K}\alpha/\text{K}\beta$ XES. A schematic of the experimental configuration is shown in Fig. 1B. Three signals were detected simultaneously as a function of pump-probe delay: (1) WAXS with a scattering range of 0.5 – 5.0 \AA^{-1} , (2) XES over the full Fe $\text{K}\beta$ spectral energy range (7035 – 7070 eV) and (3) intensity at a fixed emitted photon energy of 6404.3 ± 0.2 eV corresponding to the maximum of the $\text{K}\alpha_1$ XES peak (Fig. 1C-D). Unexpectedly, for time delays of < 1 ps the $\text{K}\alpha$ XES signal displays a clear oscillatory component, potentially present in the $\text{K}\beta$ XES (Fig. 1E, inset). These oscillations are visible also in the WAXS signal and they have been observed previously in UV-visible pump-probe measurements (Supplementary Information of Ref. [42]). Both WAXS and XES oscillations are in-phase and have the same period, providing clear evidence the oscillations originate from the same dynamical source. In order to comprehensively understand the dynamics underlying these oscillatory features, we proceed by combined quantitative analysis of all three detected signals. Firstly, we will determine the excited-state population dynamics of $[\text{Fe}(\text{bmip})_2]^{2+}$ molecules based on Fe $\text{K}\alpha/\text{K}\beta$ XES. Secondly, the accompanying structural dynamics is characterized with WAXS. Thirdly, the excited-state population and structural dynamics will be combined with quantum chemical calculations of Fe $\text{K}\alpha$ XES.

Excited-state population analysis of XES As mentioned in the introduction, both Fe $\text{K}\alpha/\text{K}\beta$ XES have a well-established sensitivity to Fe oxidation and spin state. By comparing the shape of the measured $\text{K}\beta$ XES difference spectrum with the spectra of various Fe complexes from previous studies [10,14], we can immediately exclude high spin $3d^6$ or $3d^5$ excited state

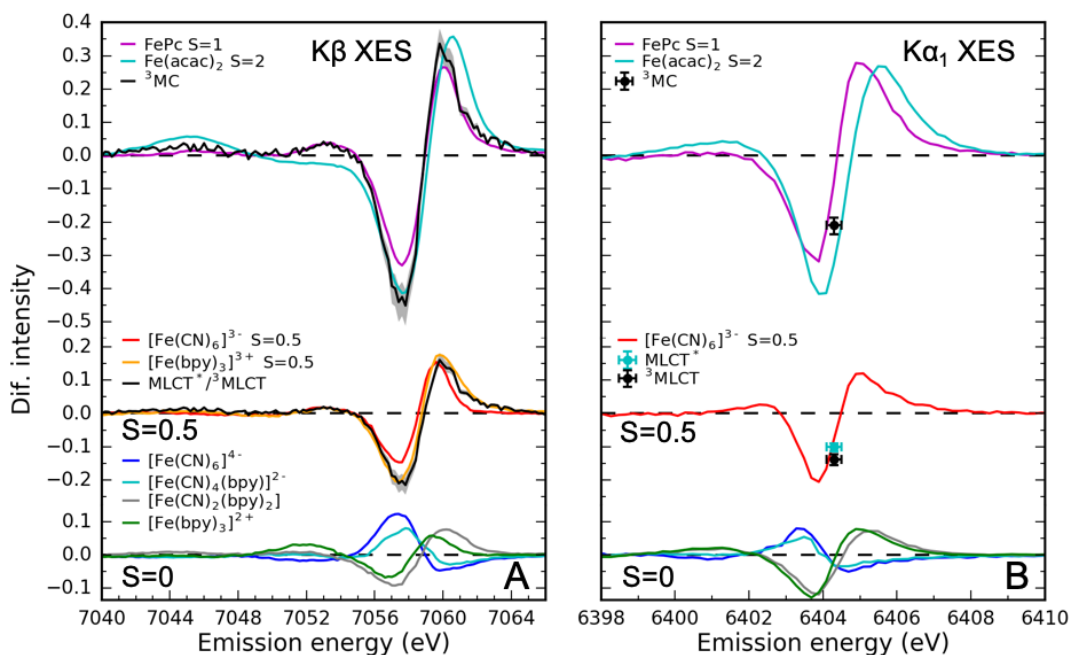


Fig. 2. Electronic state and ligand dependence of (A) K β and (B) K α difference spectra of various Fe complexes (S – nominal spin of the Fe center; bpy = 2,2'-bipyridine, Pc = phthalocyanine, acac = acetylacetonate). Difference spectra are calculated by subtracting the ground state spectrum of $[\text{Fe}(\text{bimip})_2]^{2+}$ ($S=0$). K β XES difference spectra (black lines) and K α difference intensities (black/cyan dots) of MLCT ($S=0.5$) and ^3MC ($S=1$) $[\text{Fe}(\text{bimip})_2]^{2+}$ excited states are retrieved from the XES fit described in the main text. Shaded area corresponds to the fits with excitation yield within the range of 74 – 94%. Full spectra are included in the Supplementary Information.

configurations because of the lack of a K β' feature at 7045 eV (Fig. 2A). This distinguishes $[\text{Fe}(\text{bimip})_2]^{2+}$ from an analogous complex with *t*-butyl side-groups on the ligands where the high spin $3d^6$ excited state forms following MLCT excitation [49]. Instead, the dominant K β XES difference signal shows a blue shift of the main K $\beta_{1,3}$ peak at 7058 eV. Such a shift with respect to the low-spin Fe $3d^6$ ground state is consistent with $^1\text{MLCT}/^3\text{MLCT}$ excited states, as both form a low-spin $3d^5$ doublet from the Fe perspective [11] or with a $3d^6$ intermediate spin ^3MC excited state [14]. This is evident also from the comparison with $S=0.5$ and $S=1$ model complexes in Fig. 2A (S – nominal spin of the Fe). Note, the difference spectra generated by the subtraction of the Fe singlet ground state from the Fe doublet and triplet configurations have similar spectral shapes, but the $S=1$ difference XES difference spectrum amplitude is about twice the amplitude of the $S=0.5$ difference spectrum. Because the XES difference spectra of these states effectively differ only by their amplitude, assignment between these two requires the quantitative analysis of the K α /K β XES presented below.

The K β XES difference signal does not show any significant time dependent spectral shape changes (Fig. 1D). Therefore, we focus here on the analysis of the spectral intensities at the region of biggest difference signal between 7056 – 7058.5 eV, together with the K α XES intensity recorded at 6404.3 eV (Fig. 3). The time-dependence of the K α XES intensity follows almost exactly the K β XES dynamics. Close inspection of both signals reveals that the excited state population dynamics cannot be described by a single excited state. Firstly, both XES time traces show an exponential rise in amplitude, demonstrating that at least a fraction of the initial photoexcited MLCT state transitions to a state with a larger absolute difference signal on the 100 fs timescale. Secondly, the relaxation dynamics to the electronic ground state are biexponential, with the faster decrease in the intensity decaying with a 1 – 2 ps time constant, followed by a slower decay with a ~ 10 ps time constant. We have constructed a kinetic model capable of capturing all these features. Within this model, the initially photoexcited MLCT* state branches into a ^3MC and a long-lived MLCT state, which subsequently decay with different time-constants to the electronic ground state (similar kinetics were recently also observed in another Fe-carbene complex [50]). Based on the absence of stimulated emission, prior UV-visible pump-probe measurements have assigned the long-lived MLCT to a $^3\text{MLCT}$ (note, $^1\text{MLCT}$ and $^3\text{MLCT}$ have the same Fe XES spectra)

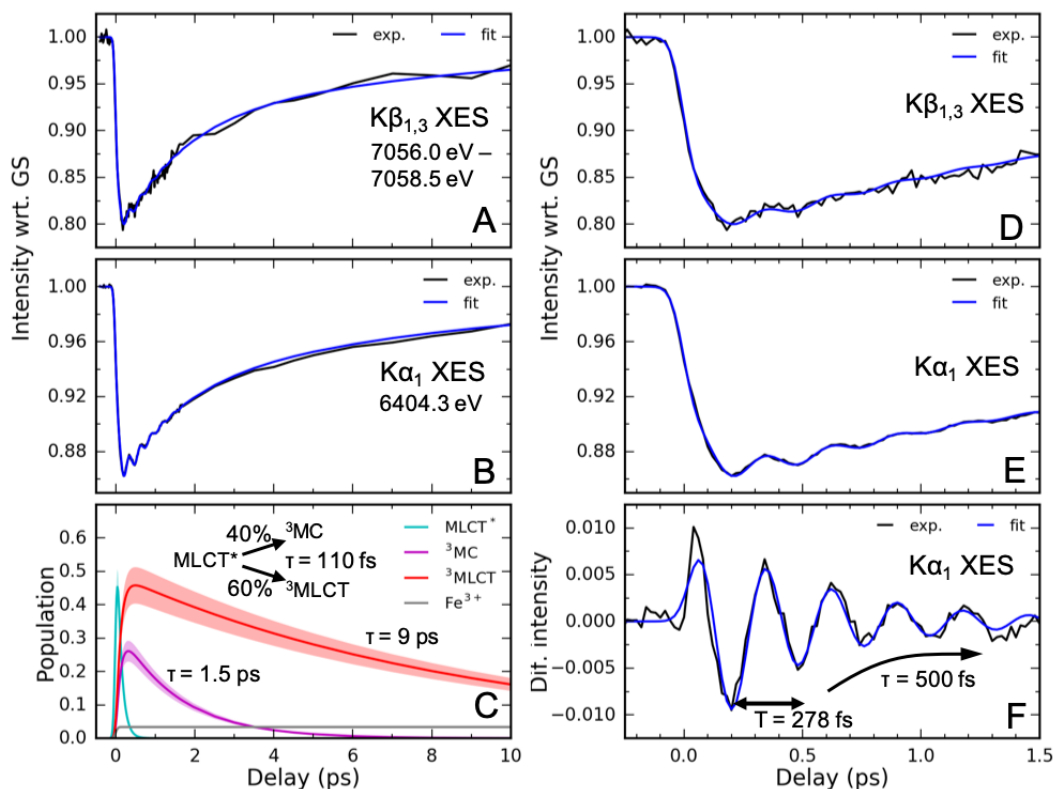


Fig. 3. Combined analysis of the time-resolved $K\beta$ and $K\alpha$ XES data. (A-B) Fits of XES time dependence with the three-state branching model discussed in the main text. (C) Electronic excited states populations derived from the fit with 84% excitation yield (shaded area corresponds to excitation yield range of 74 – 94%). (D-E) Fits of early time dynamics exhibiting oscillatory signal. (F) Oscillatory $K\alpha$ XES signal after subtraction of the non-oscillatory part.

[42]. Using this kinetic model, we carried out simultaneous fitting of the $K\alpha$ and $K\beta$ XES traces. We did not impose any constraints on the MLCT*, $^3\text{MLCT}$, ^3MC , or the ground state (GS) relative intensities, except for requiring the MLCT* and $^3\text{MLCT}$ $K\beta$ intensities to be equal. The excitation yield was fixed to $84\pm 10\%$, determined from a reference sample in identical laser fluence conditions (see Supplementary Information, SI). At this high excitation yield, analysis of the XES data at time delays >100 ps revealed 4% of the excited molecules do not decay back to the GS (Fe^{3+} population in Fig. 3C resulting from two-photon ionization of $[\text{Fe}(\text{bmip})_2]^{2+}$). However, all other aspects of the kinetic model used to fit the XES signal can be used to fit optical transient absorption data over a range of lower fluence, demonstrating the high optical laser fluence does not transform the relaxation dynamics of $[\text{Fe}(\text{bmip})_2]^{2+}$, as discussed in detail in the SI. The XES fitting found that the MLCT* decays with 110 ± 10 fs time constant with $40\pm 10\%$ ^3MC yield and $60\pm 10\%$ $^3\text{MLCT}$ yield. Subsequently both states decay into the GS, with time constants of 1.5 ± 0.5 ps and 9 ± 1 ps, respectively (Fig. 3C). A comparison of the extracted XES intensities of the transient states with the various Fe model complexes confirms the assignment of the $^3\text{MLCT}$ and the ^3MC states (Fig. 2). The change in the XES difference signal for the ^3MC state is approximately twice the difference signal associated with the MLCT states, although the intensities of the extracted transient ^3MC and MLCT XES spectra do not match exactly with the model spectra. This can be readily explained by the 5-10% changes in the XES intensity due to different ligand environments, as seen for the ground state spectra of different low-spin Fe polypyridyl and cyanide complexes with $S=0$ and $S=0.5$ spin states (Fig. 2). Additionally, the ^3MC and the $^3\text{MLCT}$ states have distinct WAXS signals due to their different structure. In the next section, we will show that the WAXS dynamics also require population of two states with

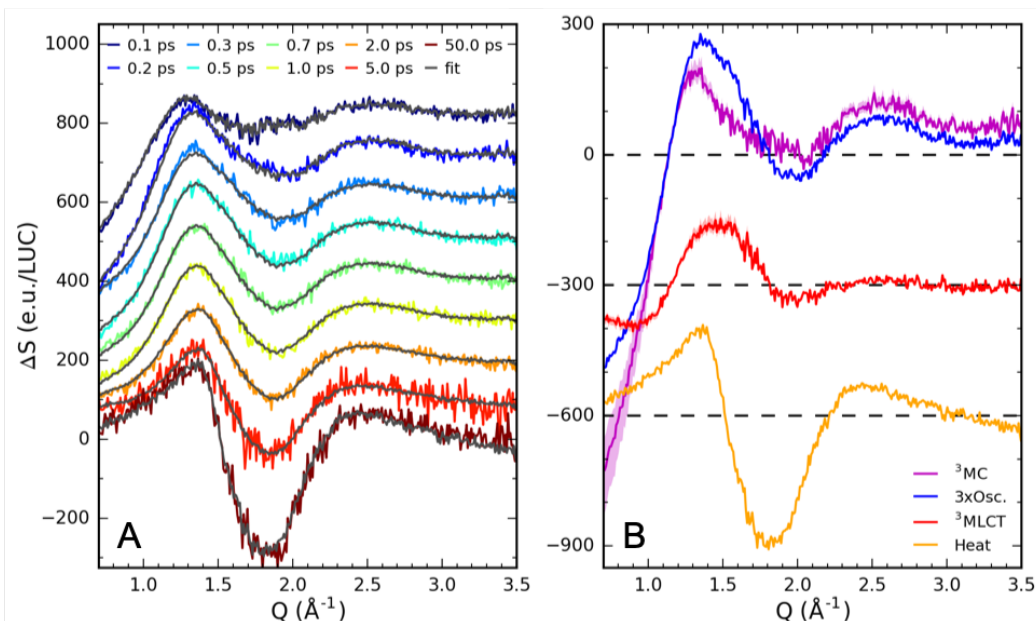


Fig. 4. Global fit of the time-resolved isotropic WAXS data based on the SVD. (A) Difference WAXS scattering signals (colored lines) and fits (black lines) at selected time delays (offset step 100 e.u./LUC). (B) Difference WAXS signals of the time-dependent components derived from global analysis: ^3MC scattering signal (magenta), oscillatory signal (blue, scaled by factor of 3), $^3\text{MLCT}$ signal (red) and MeCN heating signal (orange). All signals are normalized to electronic units per liquid unit cell (e.u./LUC).

different Fe-ligand bond lengths and lifetimes, consistent with the ^3MC and the $^3\text{MLCT}$ states and the kinetic model derived from the XES.

Simultaneously with the excited state population analysis, we fitted the oscillatory signal. This signal is described by an exponentially damped harmonic oscillation, convolved with the instrument response function (100 fs FWHM) and the 110 fs exponential decay of the MLCT*. Fitting yields a period of 278 ± 2 fs, with a damping constant of 500 ± 100 fs (Fig. 3F). The $\text{K}\beta$ XES spectra show very weak and inconclusive oscillatory dynamics (see SI). Given the order of magnitude worse signal to noise for $\text{K}\beta$ XES, compared to the $\text{K}\alpha$ signal, the absence of a clear oscillatory signal may predominantly result from a difference in the count rates for $\text{K}\alpha$ and $\text{K}\beta$ emission due to the larger $\text{K}\alpha$ cross-section and the differences in the $\text{K}\alpha$ and $\text{K}\beta$ spectrometer designs.

WAXS global analysis Time-resolved WAXS signals from solutions can be categorized into two groups: (1) solute related dynamics, including changes in the solute and the solute-solvent pair-distribution functions and (2) bulk solvent structure, typically described by changes in temperature and density [51,52]. The WAXS difference signal for time delays following solute electronic excited states relaxation are dominated by the latter contribution. Specifically, the observed broadening of the bulk acetonitrile (MeCN) scattering feature at 1.8 \AA^{-1} after time delays >5 ps corresponds to the heating of the solvent (Fig. 1C) [53]. However, for the purposes of the present study, we focus on the structural dynamics associated with changes in the solute and solute-solvent pair distribution functions. Within 100 fs, a strongly negative difference scattering signal appears below 1.0 \AA^{-1} , as well as a weakly positive signal between $1.25 - 1.75 \text{ \AA}^{-1}$ (Fig. 1C). The negative low- Q signal indicates expansion of the Fe-ligand bond lengths, similar to previously observed WAXS signals associated with the elongated metal-ligand bond lengths of MC excited states in polypyridine metal complexes [19,23,25]. Additionally, this WAXS signal exhibits the same dynamical behavior observed in the Fe $\text{K}\alpha/\text{K}\beta$ XES difference signals. In particular, the solute WAXS signal decays to the ground state biexponentially, consistent with the population of two excited states. However, because of the overlapping of solute and solvent WAXS contributions, direct comparison of

the XES and WAXS difference signals is difficult. To facilitate this comparison, and to separate the WAXS signal into components with distinct dynamics, we carry out a global analysis of the time-resolved WAXS data.

Global analysis of the WAXS difference data in Fig. 4 is based on the electronic state populations derived from the XES and the singular value decomposition (SVD) of the 2-dimensional WAXS data [54]. We fix the ^3MC and MLCT populations and the oscillatory component to be exactly the same as found from the fitting of $K\alpha/K\beta$ XES (Fig. 2). This facilitates assignment of the structural signals to specific electronic states and ensures consistency with the XES analysis, without imposing any functional form of the related Q -dependent WAXS signals. Since the difference scattering components used in the global analysis come from the SVD of the WAXS data, this does not represent a fit to a specific structural model for the solute or the solute-solvent pair distribution function. The time-dependent component needed to describe heating of the MeCN solvent is retrieved through the following procedure. The Q -dependent WAXS solvent heating signal is taken to be equal to the average WAXS difference signal between 50 – 500 ps, a time range where the MLCT and ^3MC solute related signals have vanished (the photoionized solute signal is by a factor of 100 smaller than the heating signal and therefore the late WAXS signal accurately describes hot solvent). Subsequently, by fitting the amplitude of this signal at each time delay, we find that the increase of solvent temperature can be described by two parallel exponential time constants of 0.35 ps and 13.2 ps (SI). With these four time-dependent components it is possible to accurately fit the dynamics observed for >200 fs time delays in the WAXS. We find that the <200 fs structural dynamics cannot be captured by the population dynamics of the MLCT* due to both solvent and solvation contributions to the difference signal that we have not included in the structural model (SI). However, these early dynamics do not influence the analysis of the solute dynamics at later times.

The extracted WAXS signals associated with the individual dynamical components are displayed in Fig. 4B. Firstly, the WAXS signal of the ^3MC state below 1 \AA^{-1} is about 6 – 8 times more negative than the $^3\text{MLCT}$ signal. This is consistent with significantly elongated metal-ligand bond lengths of the ^3MC state ($\sim 0.1 \text{ \AA}$ increase), whereas the $^3\text{MLCT}$ excited states metal-ligand elongation is significantly smaller ($\sim 0.01 \text{ \AA}$ increase). We verify this by simulating the ^3MC WAXS signal in the next section and confirm the assignment identified in the XES analysis. Secondly, the shapes of the WAXS signals associated with the ^3MC population and the oscillations are rather similar (Fig. 4B). This is a strong indication that the oscillations originate from structural dynamics on the ^3MC potential energy surface (PES). In addition, given the small amplitude of the $^3\text{MLCT}$ WAXS signal, it is not possible that the observed oscillations originate from nuclear wavepacket dynamics on the $^3\text{MLCT}$ PES. We, therefore, conclude that the observed oscillations originate from the dynamics on the ^3MC PES and we proceed with a quantitative modelling of these structural motions.

Table 1. Calculated distances between Fe and the coordinating atoms in the relevant $[\text{Fe}(\text{bmip})_2]^{2+}$ electronic states from Fredin *et al.* [46].

Electronic state	Fe-C distance (Å)	Fe-N distance (Å)	Average Fe-L distance, R (Å)
^1GS	1.952	1.924	1.943
$^3\text{MLCT}$	1.984	1.919	1.962
^3MC	1.977 2.087	2.062 2.205	2.066

Simulation of the ^3MC structural dynamics In order to simulate the experimental ^3MC WAXS signals we utilize the calculated DFT molecular structures from Fredin *et al.* [46]. As expected, both Fe-C and Fe-N bond lengths are significantly elongated at the ^3MC state and the average Fe-ligand bond length is increased by $\Delta R=0.123$ Å (Table. 1). In addition, there is a noticeable pseudo-Jahn-Teller effect in the ^3MC , resulting in different Fe-ligand bond lengths for the bmip ligands. The dependence of the simulated difference WAXS signal from the average Fe-ligand distance in an R range from 1.94 to 2.19 Å is shown in Fig. 5A. The simulation includes changes in the structure of the solute and in the solute-solvent pair-distribution functions (the so-called solvent cage term). The contribution of the solute was calculated by modifying the structure of $[\text{Fe}(\text{bmip})_2]^{2+}$ along the coordinate connecting the optimal GS and ^3MC structures (the GS- ^3MC coordinate). WAXS signals from these structures were calculated using the Debye scattering equation. The effect of the solvent cage was quantified with a molecular dynamics simulation of the optimal GS and ^3MC $[\text{Fe}(\text{bmip})_2]^{2+}$ structures embedded in MeCN. Solute-solvent radial distribution functions retrieved from this molecular dynamics simulation were then used to calculate the WAXS solvent cage signal [55]. Following Biasin *et al.* [19], we assume a solvent cage scattering signal proportional to ΔR . This establishes a framework for fitting the difference scattering signal associated with the ^3MC excited state over the full range of Fe-ligand distances relevant for the dynamics.

In order to simulate the WAXS signal of a nuclear wavepacket moving on the ^3MC PES, we calculated the distribution $g(R,t)$ of a Gaussian wavepacket on a harmonic PES with a vibrational period of 278 fs and a minimum at the ^3MC geometry $R=2.066$ Å (Fig. 5B). The ^3MC state is populated with 110 fs time constant at the location of the ground state geometry ($R=1.943$ Å) with zero velocity. We assign the damping of the coherent wavepacket motion, characterized by a 500 fs time constant, primarily to dephasing caused by quasi-elastic scattering. Likely, intramolecular vibrational energy distribution also contributes to the damping, but vibrational cooling to the solvent should not be a dominant cause of damping because vibrational cooling occurs on the few-to-many picosecond time scale in MeCN. Note

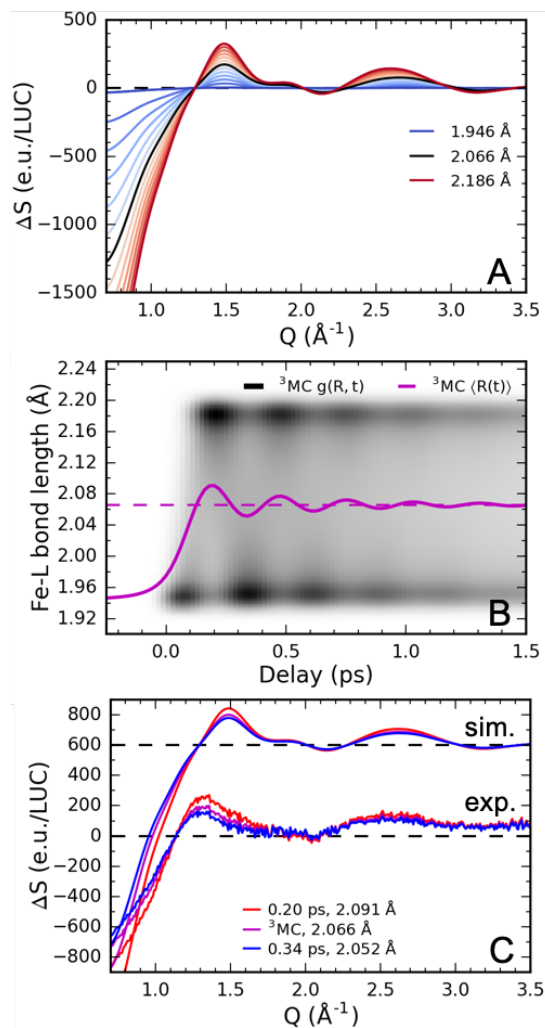


Fig. 5. Calculated solute difference WAXS signals and simulation of the oscillatory signal. (A) Dependence of $[\text{Fe}(\text{bmip})_2]^{2+}$ ^3MC difference WAXS signal from the average Fe-ligand bond length (including solute-solvent scattering). Black line corresponds to the optimal ^3MC structure. (B) Simulated ^3MC bond lengths distribution $g(R,t)$ as a function of time and the corresponding ensemble average Fe-ligand bond length (magenta). (C) Simulation of the time-dependent ^3MC difference signal and comparison to the experimental ^3MC signal extracted from the global fit (including the oscillatory component).

however, that the observed WAXS signal is primarily sensitive to the ensemble averaged Fe-ligand distance $\langle R(t) \rangle$ and not to the actual distribution of structures (SI). Comparison of the resulting simulated ^3MC difference WAXS signals with the experimental ^3MC signal extracted from the global fit shows qualitative agreement (Fig. 5C) and the observed vibrational period agrees well with a calculated low-frequency normal-mode vibration involving Fe-ligand stretching [47]. At present, we do not have a robust model for changes in the solute-solvent pair distribution function. This precludes the quantitative extraction of the Fe-ligand bond length from the WAXS signal, but does not preclude the qualitative conclusion that significant Fe-ligand bond expansion and oscillation does occur, consistent with motion on the ^3MC excited state potential energy surface [46,47]. We, therefore, conclude that the observed coherent structural dynamics can be described by a harmonic Gaussian wavepacket motion along an Fe-ligand stretching coordinate on the ^3MC PES.

Origin of the XES sensitivity to nuclear wavepacket oscillations We carried out *ab initio* Restricted Active Space Self-Consistent Field (RASSCF) calculations of the ^3MC excited state $\text{K}\alpha$ XES spectra as a function of average Fe-ligand bond length R to establish the XES sensitivity to the structural dynamics of the molecule. $\text{K}\alpha$ XES spectra of four $[\text{Fe}(\text{bmip})_2]^{2+}$ molecular structures were calculated, corresponding

to the optimal ground state ($R=1.943 \text{ \AA}$) and the ^3MC ($R=2.066 \text{ \AA}$) geometries, as well as for one elongated ($R=2.092 \text{ \AA}$) and one contracted ($R=2.050 \text{ \AA}$) ^3MC structure (Fig. 6A, only two spectra are shown for clarity). We find that the structural effect can be described by an energy shift of the spectrum, without any significant change to the shape. The shift of the spectrum is linear with respect to the Fe-ligand distance and has a magnitude of $\Delta E/\Delta R = 0.3 \text{ eV}/0.123 \text{ \AA}$ (corresponding to a change from GS to ^3MC geometry for the ^3MC electronic state). At the emitted photon energy where the $\text{K}\alpha$ XES data was recorded (6404.3 eV), these calculations indicate that such Fe-ligand bond elongation leads to a linear decrease in the ^3MC intensity with a slope of $\Delta I/\Delta R = 10\%/0.123 \text{ \AA}$ (relative to the ground state intensity, Fig. 6B). By considering the linear intensity dependence at 6404.3 eV, we can simulate the $\text{K}\alpha$ XES signal based on the ^3MC nuclear wavepacket dynamics ($g(R,t)$ in Fig. 5B). We keep all the other populations and relative intensities fixed at the values found from the XES fitting (Fig. 3), except a small decrease in the MLCT* intensity to compensate for the increase in the ^3MC intensity due to the XES red shift for shorter Fe-ligand distances. We find that agreement with the experimental $\text{K}\alpha$ XES time trace is achieved if $\Delta I/\Delta R = 16\%/0.123 \text{ \AA}$ (Fig. 6C). This

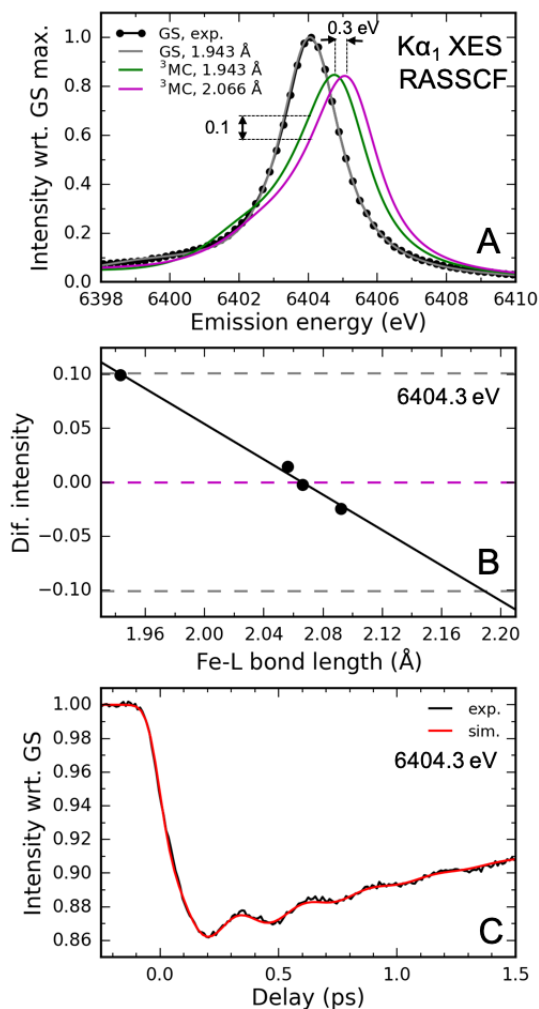


Fig. 6. Calculated $\text{K}\alpha$ XES spectra and simulation of the oscillatory signal. (A) Calculated XES spectra of the $[\text{Fe}(\text{bmip})_2]^{2+}$ ground state (gray) and ^3MC excited state at different geometries (magenta and green). (B) RASSCF ^3MC excited state XES intensity change as a function of the Fe-ligand bond length (relative to the optimal ^3MC structure). (C) Simulation of $\text{K}\alpha$ XES time-dependent intensity.

structural sensitivity is in reasonable agreement with the value derived from the RASSCF simulations. Additionally, we note that the ligand environment dependent $K\alpha$ and $K\beta$ spectra of cyanide/bipyridine $S=0/S=0.5$ model complexes exhibit the same trend (Fig. 2). The dominant ligand dependent effect is an overall shift of the spectrum, and weakening of the ligand field shifts the spectrum to higher emission energies. Similarly, the magnitude of the effect close to the maximum of the spectrum is $\sim 10\%$.

Discussion

We have attained a detailed picture of coupled electronic and nuclear structural dynamics during photoinduced electron transfer in an Fe carbene, $[\text{Fe}(\text{bmip})_2]^{2+}$, photosensitizer using the complementary sensitivities of XES and WAXS. We found that the directly photoexcited MLCT* state follows two distinct relaxation pathways (Fig. 7, lower half). 60% of the population relaxes to a $^3\text{MLCT}$ excited state and decays with a 9 ps time constant. About 40% of the MLCT* population relaxes to a ^3MC state via ultrafast non-adiabatic back-electron transfer to Fe. This ^3MC decays to the ground state with 1.5 ps. The observation of a 9 ps $^3\text{MLCT}$ state confirms the previous assignment based on the UV-visible transient absorption experiments with 485 nm excitation wavelength, although the UV-visible experiments did not detect any ^3MC population [42]. Importantly, when the complex is excited at 400 nm and probed in the UV-visible, the data can be fit with the same kinetic parameters used to model the XES data (SI). This supports the conclusion that the branching ratio between $^3\text{MLCT}$ and ^3MC formation depends on the pump photon energy.

Recently, similar excited state relaxation dynamics were observed in a related heteroleptic $[\text{Fe}(\text{bpy})(\text{btz})_2]^{2+}$ complex [bpy=2, 2'-bipyridine, btz= 4,4'-bis(1,2,3-triazol-5-ylidene)] [50]. It was determined for this complex that the $^3\text{MLCT}$ state decay is mediated by the ^3MC state. Because $[\text{Fe}(\text{bmip})_2]^{2+}$ has a slightly longer $^3\text{MLCT}$ and a slightly shorter ^3MC lifetime than $[\text{Fe}(\text{bpy})(\text{btz})_2]^{2+}$, we cannot experimentally distinguish between $^3\text{MLCT} \rightarrow ^3\text{MC} \rightarrow \text{GS}$ or $^3\text{MLCT} \rightarrow \text{GS}$ relaxation pathways here (SI). Given the otherwise similar population dynamics in these complexes, it is likely that the ^3MC state facilitates the $^3\text{MLCT}$ decay also in $[\text{Fe}(\text{bmip})_2]^{2+}$. Ultrafast $^1,^3\text{MLCT} \rightarrow ^3\text{MC}$ population transfer has been observed before in Fe^{2+} coordination complexes [10,14], but only in iron carbenes has ultrafast ^3MC formation co-existed with a long-lived $^3\text{MLCT}$ state. Intuitively, this would require that the MLCT* is resonant with the ^3MC state, whereas the $^3\text{MLCT}$ is lower in energy with a small barrier between the $^3\text{MLCT}$ and ^3MC . In Fig. 7 we show qualitative potential energy surfaces consistent with this explanation. There, 400 nm light excites the molecule high in the MLCT manifold. The subsequent branching is likely governed by a competition between electron transfer to the ^3MC and relaxation within the MLCT manifold. Coupling to

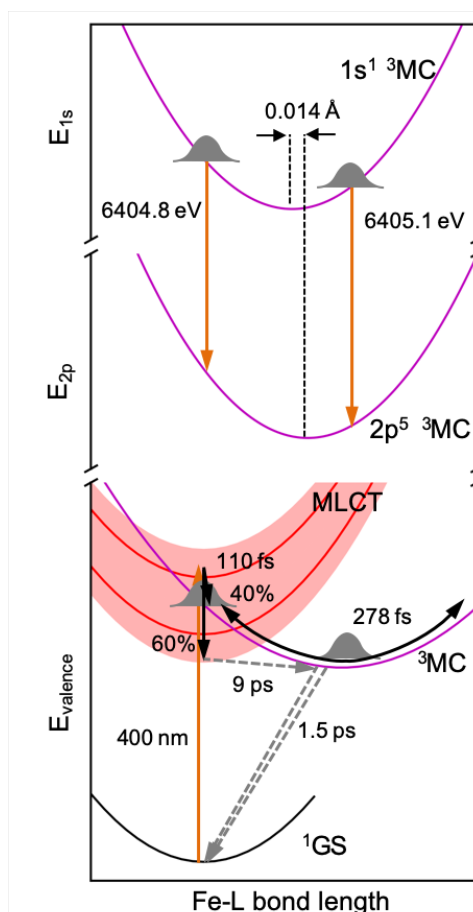


Fig. 7. Photoinduced electron transfer dynamics of $[\text{Fe}(\text{bmip})_2]^{2+}$ and the origin of XES structural sensitivity due to core-level vibronic coupling between 1s and 2p core-ionized states. Potential energy surfaces are qualitative.

different MC states, as well as the initial excitation wavelength could influence the branching ratio [56]. Recently, a branching between the ^3MC and $^3\text{MLCT}$ populations has been predicted for $[\text{Fe}(\text{bmip})_2]^{2+}$ by quantum dynamical simulations, although the simulated time constant of the ^3MC formation was ~ 1 ps [47]. This branching between $^3\text{MLCT}$ and ^3MC states will influence photosensitizer performance. Iron carbene photosensitizers with carboxylate-functionalized bmip ligands has demonstrated a charge injection efficiency of 92% to TiO_2 nanoparticles [45]. Interestingly, this electron injection yield exceeds the $^3\text{MLCT}$ yield we observe for $[\text{Fe}(\text{bmip})_2]^{2+}$ dissolved in acetonitrile. Given the expected sensitivity of the branching ratio to small changes in the potential energy landscape, the higher yield for charge injection could result from the red shifted MLCT energies of the COOH-functionalized Fe carbene photosensitizer, differences in the solvation response [57], and the potential for electron injection of electrons from ^3MC excited states. In summary, the observed population dynamics highlight the critical role of ^3MC excited states in the MLCT relaxation of $[\text{Fe}(\text{bmip})_2]^{2+}$.

The time-resolved WAXS analysis for the ^3MC excited state shows Fe-ligand bond expansion consistent with an average Fe-ligand bond length increase of $\Delta R = 0.123$ Å predicted by theory [46]. Since the electron transfer from MLCT* to the ^3MC excited state occurs with a 110 fs time constant, impulsive compared to the 278 fs period of Fe-ligand stretching mode, relaxation from the MLCT* excited state to the ^3MC state generates a vibrational wavepacket along this coordinate. Periodic modulation of the Fe-ligand bond length on the ^3MC PES are clearly captured with WAXS. Additionally, these nuclear dynamics lead to oscillations in the $\text{K}\alpha$ XES signal. Based on an *ab initio* RASSCF calculation we can establish that this structural sensitivity results from a linear shift of the XES spectrum as a function of the Fe-ligand bond length. The linear change in energy is a manifestation of first order vibronic coupling between the core-levels, resulting in a relative displacement of the 1s and 2p core-ionized PESs along the coordinate of the ^3MC wavepacket motion (Fig. 7, upper half). The calculated RASSCF core-ionized PESs show noticeable shortening and stiffening of the Fe-ligand bond in comparison to the ^3MC state without a core-hole (SI). This is due to stabilization of the Fe 3d levels upon the creation of the core hole, which leads to improved overlap with the occupied ligand orbitals. Most importantly, this core-hole induced electronic relaxation is slightly different for 1s and 2p core-holes. Even though the force constant k_{core} of the Fe-ligand stretching coordinate in the presence of either a 1s or 2p core-ionization is the same, the calculated optimal bond length is longer for the 2p state, with displacement $\Delta R_{\text{core}} = 0.014$ Å (0.7% relative to the ^3MC optimal bond length, Fig. 7). It follows that the energy difference between the core-ionized PESs changes with a slope of $\kappa_{\text{core}} = k_{\text{core}} \Delta R_{\text{core}}$ (see SI). Here κ_{core} is the first-order vibronic coupling constant of the $(2p^5)^3\text{MC}$ states with respect to the $(1s^1)^3\text{MC}$ states [58]. Based on the calculated $\text{K}\alpha$ XES shift, we find that $\kappa_{\text{core}} = 2.44$ eV/Å. It is relevant to compare this *dynamic* shifting effect to a text-book *static* broadening effect of vibronic coupling. Considering that the calculated core-ionized PESs vibrational period is 241 fs ($h\nu = 17$ meV), the corresponding Huang-Rhys parameter between the core-levels is $S_{\text{core}} \approx 1$. Because the 1s core-hole lifetime is < 1 fs, we can neglect any nuclear dynamics induced by the core-hole. Therefore, one can estimate the vibronic broadening to be 40 meV (FWHM). In contrast, the overall $\text{K}\alpha_1$ XES broadening is equal to about 1.55 eV (FWHM), dominated by the natural lifetime of 1s and $2p_{3/2}$ states. It is evident that such a small vibronic broadening relative to the lifetime broadening is not detectable in the width of a static $\text{K}\alpha$ XES spectrum. Importantly, one is significantly more sensitive to this vibronic coupling in a time-resolved experiment, because it appears as a shift of the XES spectrum and because the wavepacket samples a wide range of bond lengths.

Prior investigations of the influence of metal-ligand bonding on Fe $\text{K}\alpha/\text{K}\beta$ XES spectra have concluded that the spectra change minimally with changes in ligand field [59,60] and exhibit small bonding dependent chemical shifts because both the initial and final state involved in X-ray emission contain a core-hole [61]. The strong iron-ligand coordination bonds present in $[\text{Fe}(\text{bmip})_2]^{2+}$ and cyano containing Fe complexes clearly present exceptions, with $\text{K}\alpha$ and $\text{K}\beta$

mainline emission peak positions exhibiting noticeable ligand dependent shifts, as shown in Fig. 2. These shifts reflect the significant variation in Fe-ligand bonding for these complexes. Specifically, $[\text{Fe}(\text{CN})_6]^{4-}$ has a 10Dq value >1 eV greater than $[\text{Fe}(\text{bpy})_3]^{2+}$ and the covalency of the t_{2g} orbitals is significantly larger ($\sim 25\%$ compared to $\sim 15\%$) [62]. For $[\text{Fe}(\text{bmip})_2]^{2+}$, the ${}^3\text{MC}$ excited state in the ground state geometry has a 10Dq ~ 1 eV more than in the optimal geometry [46,47]. As expected, this is related to significant variation in the covalency as a function of Fe-ligand bond length, with the ligand character of the e_g orbitals decreasing from 20% for the ground state geometry to 10% for the equilibrium ${}^3\text{MC}$ geometry (SI). These changes in Fe-ligand interaction result in differential screening of the 1s and 2p core holes as a function of Fe-ligand bond length and different optimal Fe-ligand bond lengths for the 1s and 2p core-ionized states (core-level vibronic coupling).

The magnitude of the core-level vibronic coupling in $[\text{Fe}(\text{bmip})_2]^{2+}$ is likely relatively large due to the strong bonding between Fe and the carbene ligands. However, the amplitude of the ensemble averaged $\langle R(t) \rangle$ oscillations are also significantly suppressed due to the fact the vibrational wavepacket is generated by the 110 fs lifetime of the MLCT* excited state, not through optical excitation of Franck-Condon active vibrational modes. Direct photoexcitation to a displaced PES would enhance the XES oscillations, possibly making the core-level vibronic effect observable also in complexes with weaker metal-ligand bonds.

Methods

Experiment Polycrystalline $[\text{Fe}(\text{bmip})_2](\text{PF}_6)_2$ was synthesized as described in Ref. [42]. The time-resolved XES and WAXS measurements were conducted at the X-ray Pump-Probe (XPP) endstation at the Linac Coherent Light Source (LCLS) [63]. The sample consisted of 20.3 mM $[\text{Fe}(\text{bmip})_2](\text{PF}_6)_2$ dissolved in anhydrous acetonitrile. A recirculating 50 μm diameter round Rayleigh jet in He environment was used for sample delivery. The sample was excited with 400 nm optical laser pulses of 45 fs duration, 120 μm focus diameter (FWHM), and 45 mJ/cm^2 fluence. 8.5 keV unmonochromatized X-ray laser pulses of 30 fs duration and 10 μm focal diameter were used to probe the sample. The Fe $\text{K}\beta$ XES was spatially dispersed using a von Hamos spectrometer consisting of four dispersive Ge(620) crystal analyzers with a central Bragg angle of 79.1 degrees [64], and detected with a 140k Cornell-SLAC Pixel Array Detector (CSPAD) [65]. The Fe $\text{K}\alpha$ XES was analyzed using a spherically bent Ge(440) crystal in Rowland geometry and detected with a second 140k CSPAD. The WAXS was detected with 2.3M CSPAD in forward scattering geometry. The relative timing between pump and X-ray probe pulses was measured for each X-ray shot [66]. The full 2D images of the XES and WAXS detectors were read out shot-to-shot and subsequently processed and binned after the pump-probe delay. XES emission energies were calibrated after ground state spectra measured at the Stanford Synchrotron Radiation Lightsource (SSRL). WAXS Q-range was calibrated with the acetonitrile heating signal [53]. WAXS data analysis procedures are described in Ref. [67] and [68].

The static Fe $\text{K}\alpha$ and $\text{K}\beta$ XES spectra of $[\text{Fe}(\text{bmip})_2](\text{PF}_6)_2$ and the model complexes were measured at the SSRL beamline 6-2. Samples were measured as powders. Monochromatic incident X-rays at 7.3 keV (double-crystal Si(311) monochromator, 0.2 eV FWHM bandwidth) were used. Identical spectrometers to the LCLS experiment with a Si drift diode detector were used. The monochromator energy was calibrated with a Fe foil and the spectrometers calibration was done using elastically scattered X-rays. $[\text{Fe}(\text{bpy})_3]^{3+}$ and FePc $\text{K}\beta$ XES spectra were taken from Ref. [10].

Theory $\text{K}\alpha$ XES spectra were calculated at four $[\text{Fe}(\text{bmip})_2]^{2+}$ geometries. The geometries for the ground state energy minimum and the ${}^3\text{MC}$ energy minimum were obtained from Ref. [46], where optimization was done at PBE0/6-311G(d,p) level and included MeCN solvent through the polarizable continuum model. Two other geometries were created on each side of the ${}^3\text{MC}$ energy minimum by changing the geometry along the GS- ${}^3\text{MC}$ coordinate, with $\Delta R = -0.016$ Å and $\Delta R = +0.026$ Å. All structures belong to the D_2 point group but as the iron is six-coordinated, O_h point group labels will be used to describe the metal orbitals. The spectra were calculated using the *ab initio* Restricted Active Space (RAS) approach in the OpenMolcas package (version v18.0.0180105-1800) [69], using a new efficient configuration interaction algorithm [70]. The electronic structure of the valence and core-ionized electronic states was evaluated at RASSCF/ANO-RCC-VDZP level of theory [71–73]. The valence active space consisted in 10 electrons distributed in 10 orbitals, the five Fe 3d dominated orbitals and five corresponding correlating orbitals. First, two filled Fe-ligand σ -bonding orbitals together with two metal-dominated e_g orbitals forming σ^* orbitals with the ligand. Second, three filled

metal-dominated non-bonding t_{2g} orbitals together with three empty Fe 4d orbitals of t_{2g} symmetry. These orbitals were placed in the RAS2 space, where all possible excitations were allowed. The Fe 1s orbital was placed in the RAS3 space, allowing for a maximum of one electron while the three Fe 2p orbitals were placed in the RAS1 space, allowing for a maximum of one hole. To model the core-ionized states and ensure the hole stayed in the core orbitals instead of higher-lying orbitals, the core hole orbitals were kept frozen in the RASSCF optimizations of the 1s and 2p core-ionized states. The valence electronic states were calculated with the singlet and triplet spin multiplicities, while the core-ionized states were calculated with doublet and quartet spin multiplicities. The RASSCF wavefunction optimizations were performed using the state average formalism with equal weighting. For the 3MC states, the 1s core hole was averaged over 9 doublet and 6 quartet states. For the 2p core-hole states 50 doublet and 18 quartet states were used. Spin-orbit coupled states were obtained using a Douglas–Kroll–Hess (DKH) Hamiltonian and atomic mean field integrals [74,75]. Transition dipole moments between the core-ionized states were calculated with the RAS state interaction (RASSI) method [76]. For comparison to experiment, RAS spectra were broadened with a Gaussian of 0.6 eV (FWHM) and Lorentzian function of 1.55 eV (FWHM). The spectrum at the GS geometry was shifted to align with the experimental emission maximum. The same shift was then used for all calculated spectra. The sensitivity of the results with respect to adding dynamic correlation through second-order perturbation theory was tested for the GS and 3MC geometries [77]. The energy difference between the two emission maxima increased by 0.12 eV, while the emission intensity of the 3MC state increased by 5% relative to that of the ground state. These two effects largely cancel when calculating the intensity at the GS emission maximum.

Acknowledgements

Work by KK, MER, and KJG were supported by the U.S. Department of Energy, Office of Science, Basic Energy Sciences, Chemical Sciences, Geosciences, and Biosciences Division. Use of the Linac Coherent Light Source (LCLS) and the Stanford Synchrotron Radiation Lightsource, SLAC National Accelerator Laboratory, is supported by the U.S. Department of Energy, Office of Science, Office of Basic Energy Sciences under Contract No. DE-AC02-76SF00515. ML acknowledges financial support from the Knut and Alice Wallenberg Foundation (grant no. KAW-2013.0020) and Olle Engkvists stiftelse. TCBH, EB, MGL, MP, KBM, and MMN gratefully acknowledge support by the Danish Council for Independent Research under grant no. DFF-4002-00272B. MIP, MMN, and KBM acknowledge support by the Danish Council for Independent Research under grant no. DFF-8021-00347B. This work has been supported by the Danish Council of Independent Research Grant No. 4002-00272 and the Independent Research Fund Denmark Grant No. 8021-00347B. KH, KSK, MMN, PV, TBVD, MGL, MC and FBH are highly grateful to DANSCATT for supporting the beamtime activities. SEC gratefully acknowledges funding from the Helmholtz Recognition Award. The ELI-ALPS project (GINOP-2.3.6-15-2015-00001) is supported by the European Union and co-financed by the European Regional Development Fund. JU acknowledges support from the Knut and Alice Wallenberg Foundation and from the Carl Tryggers Foundation. SK acknowledges the support from Knut & Alice Wallenberg foundation (KAW 2014.0370). DSS, EB, and GV acknowledge support from the ‘Lendület’ (Momentum) Program of the Hungarian Academy of Sciences (LP2013-59), the Government of Hungary and the European Regional Development Fund under grant No. VEKOP-2.3.2-16-2017-00015, the European Research Council via contract ERC-StG-259709 (X-cited!), the Hungarian Scientific Research Fund (OTKA) under contract K109257, and the National Research, Development and Innovation Fund (NKFIH FK 124460). ZN acknowledges support from the Bolyai Fellowship of the Hungarian Academy of Sciences.

Author contributions

KK and KJG wrote the manuscript with input from all the authors. TCBH, KSK, KH, TBVD, KK, EB, PC, RWH, MER, MGL, FBH, PV, MC, ZN, DSS, EB, RAM, JMG, SN, MS, DS, HTL, SC, MMN, GV and JU carried out the LCLS experiment. KK, SK and MER carried out the SSRL experiments. KK and KSK analyzed the XES data. KH, KK, LS and MGL analyzed the WAXS data. JU measured and KK analyzed the optical transient absorption data. MV, ML, EK and MD carried out the RASSCF calculations. EB carried out the molecular dynamic simulation. YL, HT, CT and KW synthesized the sample.

Data availability

The experimental time-resolved WAXS and XES data underlying Figs 1, 3, and 4 are provided as a Source Data file. All relevant data and programs that support the findings of this study are available from the authors on reasonable request.

References

- [1] A.H. Zewail, Femtochemistry: Atomic-scale dynamics of the chemical bond, *J. Phys. Chem. A*. 104 (2000) 5660–5694. doi:10.1021/jp001460h.
- [2] H.J. Wörner, C.A. Arrell, N. Banerji, A. Cannizzo, M. Chergui, A.K. Das, et al., Charge migration and charge transfer in molecular systems, *Struct. Dyn.* 4 (2017) 061508. doi:10.1063/1.4996505.
- [3] Y. Liu, P. Persson, V. Sundström, K. Wärnmark, Fe *N*-Heterocyclic Carbene Complexes as Promising Photosensitizers, *Acc. Chem. Res.* 49 (2016) 1477–1485. doi:10.1021/acs.accounts.6b00186.
- [4] O.S. Wenger, Is Iron the New Ruthenium?, *Chem. - A Eur. J.* 25 (2019) 6043–6052. doi:10.1002/chem.201806148.
- [5] J.K. McCusker, Electronic structure in the transition metal block and its implications for light harvesting, *Science* (80-.). 363 (2019) 484–488. doi:10.1126/science.aav9104.
- [6] C.S. Ponseca, P. Chábera, J. Uhlig, P. Persson, V. Sundström, Ultrafast Electron Dynamics in Solar Energy Conversion, *Chem. Rev.* 117 (2017) 10940–11024. doi:10.1021/acs.chemrev.6b00807.
- [7] M. Chergui, Ultrafast Photophysics of Transition Metal Complexes, *Acc. Chem. Res.* 48 (2015) 801–808. doi:10.1021/ar500358q.
- [8] M. Chergui, Time-resolved X-ray spectroscopies of chemical systems: New perspectives, *Struct. Dyn.* 3 (2016) 031001. doi:10.1063/1.4953104.
- [9] P.M. Kraus, M. Zürch, S.K. Cushing, D.M. Neumark, S.R. Leone, The ultrafast X-ray spectroscopic revolution in chemical dynamics, *Nat. Rev. Chem.* 2 (2018) 82–94. doi:10.1038/s41570-018-0008-8.
- [10] W. Zhang, R. Alonso-Mori, U. Bergmann, C. Bressler, M. Chollet, A. Galler, et al., Tracking excited-state charge and spin dynamics in iron coordination complexes., *Nature*. 509 (2014) 345–348. doi:10.1038/nature13252.
- [11] W. Zhang, K.S. Kjær, R. Alonso-Mori, U. Bergmann, M. Chollet, L.A. Fredin, et al., Manipulating charge transfer excited state relaxation and spin crossover in iron coordination complexes with ligand substitution, *Chem. Sci.* 101 (2016) 1298–1300. doi:10.1039/C6SC03070J.
- [12] K.S. Kjær, W. Zhang, R. Alonso-Mori, U. Bergmann, M. Chollet, R.G. Hadt, et al., Ligand manipulation of charge transfer excited state relaxation and spin crossover in [Fe(2,2'-bipyridine)₂(CN)₂], *Struct. Dyn.* 4 (2017) 044030. doi:10.1063/1.4985017.
- [13] M.W. Mara, R.G. Hadt, M.E. Reinhard, T. Kroll, H. Lim, R.W. Hartsock, et al., Metalloprotein entatic control of ligand-metal bonds quantified by ultrafast x-ray spectroscopy., *Science*. 356 (2017) 1276–1280. doi:10.1126/science.aam6203.
- [14] K.S. Kjær, K. Kunnus, T.C.B. Harlang, T.B. Van Driel, K. Ledbetter, R.W. Hartsock, et al., Solvent control of charge transfer excited state relaxation pathways in [Fe(2,2'-bipyridine)(CN)₄]²⁻, *Phys. Chem. Chem. Phys.* 20 (2018) 4238–4249. doi:10.1039/C7CP07838B.
- [15] H. Ihee, M. Lorenc, T.K. Kim, Q.Y. Kong, M. Cammarata, J.H. Lee, et al., Ultrafast x-ray diffraction of transient molecular structures in solution., *Science*. 309 (2005) 1223–7. doi:10.1126/science.1114782.
- [16] D. Arnlund, L.C. Johansson, C. Wickstrand, A. Barty, G.J. Williams, E. Malmerberg, et al., Visualizing a protein quake with time-resolved X-ray scattering at a free-electron laser, *Nat. Methods*. 11 (2014) 923–926. doi:10.1038/nmeth.3067.
- [17] K.H. Kim, J.G. Kim, S. Nozawa, T. Sato, K.Y. Oang, T.W. Kim, et al., Direct observation of bond formation in solution with femtosecond X-ray scattering, *Nature*. 518 (2015) 385–389. doi:10.1038/nature14163.
- [18] T.B. van Driel, K.S. Kjær, R.W. Hartsock, A.O. Dohn, T. Harlang, M. Chollet, et al., Atomistic characterization of the active-site solvation dynamics of a model photocatalyst, *Nat. Commun.* 7 (2016) 13678. doi:10.1038/ncomms13678.
- [19] E. Biasin, T.B. van Driel, K.S. Kjær, A.O. Dohn, M. Christensen, T. Harlang, et al., Femtosecond X-Ray Scattering Study of Ultrafast Photoinduced Structural Dynamics in Solvated [Co(terpy)₂]²⁺, *Phys. Rev. Lett.* 117 (2016) 013002. doi:10.1103/PhysRevLett.117.013002.
- [20] J.H. Lee, M. Wulff, S. Bratos, J. Petersen, L. Guerin, J.-C. Leicknam, et al., Filming the Birth of Molecules and Accompanying Solvent Rearrangement, *J. Am. Chem. Soc.* 135 (2013) 3255–3261. doi:10.1021/ja312513w.
- [21] M. Marcellini, A. Nasedkin, B. Zietz, J. Petersson, J. Vincent, F. Palazzetti, et al., Transient isomers in the photodissociation of bromiodomethane, *J. Chem. Phys.* 148 (2018) 134307.

- doi:10.1063/1.5005595.
- [22] E.H. Choi, D.-S. Ahn, S. Park, C. Kim, C.W. Ahn, S. Kim, et al., Structural Dynamics of Bismuth Triiodide in Solution Triggered by Photoinduced Ligand-to-Metal Charge Transfer, *J. Phys. Chem. Lett.* 10 (2019) 1279–1285. doi:10.1021/acs.jpcclett.9b00365.
- [23] D. Khakhulin, L.M. Lawson Daku, D. Leshchev, G.E. Newby, M. Jarenmark, C. Bressler, et al., Visualizing the coordination-spheres of photoexcited transition metal complexes with ultrafast hard X-rays, *Phys. Chem. Chem. Phys.* 21 (2019) 9277–9284. doi:10.1039/C9CP01263J.
- [24] S.E. Canton, K.S. Kjær, G. Vankó, T.B. van Driel, S. Adachi, A. Bordage, et al., Visualizing the non-equilibrium dynamics of photoinduced intramolecular electron transfer with femtosecond X-ray pulses., *Nat. Commun.* 6 (2015) 6359. doi:10.1038/ncomms7359.
- [25] K. Haldrup, G. Vankó, W. Gawelda, A. Galler, G. Doumy, A.M. March, et al., Guest–Host Interactions Investigated by Time-Resolved X-ray Spectroscopies and Scattering at MHz Rates: Solvation Dynamics and Photoinduced Spin Transition in Aqueous Fe(bipy) 3 2+, *J. Phys. Chem. A.* 116 (2012) 9878–9887. doi:10.1021/jp306917x.
- [26] S.E. Canton, X. Zhang, J. Zhang, T.B. van Driel, K.S. Kjaer, K. Haldrup, et al., Toward Highlighting the Ultrafast Electron Transfer Dynamics at the Optically Dark Sites of Photocatalysts, *J. Phys. Chem. Lett.* 4 (2013) 1972–1976. doi:10.1021/jz401016h.
- [27] K.S. Kjær, T.B. Van Driel, T.C.B. Harlang, K. Kunnus, E. Biasin, K. Ledbetter, et al., Finding intersections between electronic excited state potential energy surfaces with simultaneous ultrafast X-ray scattering and spectroscopy, *Chem. Sci.* 10 (2019) 5749–5760. doi:10.1039/C8SC04023K.
- [28] G. Peng, F.M.F. deGroot, K. Haemaelaenen, J.A. Moore, X. Wang, M.M. Grush, et al., High-resolution manganese x-ray fluorescence spectroscopy. Oxidation-state and spin-state sensitivity, *J. Am. Chem. Soc.* 116 (1994) 2914–2920. doi:10.1021/ja00086a024.
- [29] P. Glatzel, U. Bergmann, High resolution 1s core hole X-ray spectroscopy in 3d transition metal complexes - Electronic and structural information, *Coord. Chem. Rev.* 249 (2005) 65–95. doi:10.1016/j.ccr.2004.04.011.
- [30] G. Vankó, T. Neisius, G. Molnár, F. Renz, S. Kárpáti, A. Shukla, et al., Probing the 3d Spin Momentum with X-ray Emission Spectroscopy: The Case of Molecular-Spin Transitions, *J. Phys. Chem. B.* 110 (2006) 11647–11653. doi:10.1021/jp0615961.
- [31] G. Vankó, A. Bordage, P. Glatzel, E. Gallo, M. Rovezzi, W. Gawelda, et al., Spin-state studies with XES and RIXS: From static to ultrafast, *J. Electron Spectrosc. Relat. Phenom.* 188 (2013) 166–171. doi:10.1016/j.elspec.2012.09.012.
- [32] K. Haldrup, G. Levi, E. Biasin, P. Vester, M.G. Laursen, F. Beyer, et al., Ultrafast X-Ray Scattering Measurements of Coherent Structural Dynamics on the Ground-State Potential Energy Surface of a Diplatinum Molecule, *Phys. Rev. Lett.* 122 (2019) 063001. doi:10.1103/PhysRevLett.122.063001.
- [33] H.T. Lemke, C. Bressler, L.X. Chen, D.M. Fritz, K.J. Gaffney, A. Galler, et al., Femtosecond X-ray Absorption Spectroscopy at a Hard X-ray Free Electron Laser: Application to Spin Crossover Dynamics, *J. Phys. Chem. A.* 117 (2013) 735–740. doi:10.1021/jp312559h.
- [34] L.X. Chen, X. Zhang, Photochemical Processes Revealed by X-ray Transient Absorption Spectroscopy, *J. Phys. Chem. Lett.* 4 (2013) 4000–4013. doi:10.1021/jz401750g.
- [35] M.L. Shelby, P.J. LeStrange, N.E. Jackson, K. Haldrup, M.W. Mara, A.B. Stickrath, et al., Ultrafast Excited State Relaxation of a Metalloporphyrin Revealed by Femtosecond X-ray Absorption Spectroscopy, *J. Am. Chem. Soc.* 138 (2016) 8752–8764. doi:10.1021/jacs.6b02176.
- [36] H.T. Lemke, K.S. Kjær, R. Hartsock, T.B. van Driel, M. Chollet, J.M. Glowonia, et al., Coherent structural trapping through wave packet dispersion during photoinduced spin state switching, *Nat. Commun.* 8 (2017) 15342. doi:10.1038/ncomms15342.
- [37] N.A. Miller, A. Deb, R. Alonso-Mori, J.M. Glowonia, L.M. Kiefer, A. Konar, et al., Ultrafast X-ray Absorption Near Edge Structure Reveals Ballistic Excited State Structural Dynamics, *J. Phys. Chem. A.* 122 (2018) 4963–4971. doi:10.1021/acs.jpca.8b04223.
- [38] T. Katayama, T. Northey, W. Gawelda, C.J. Milne, G. Vankó, F.A. Lima, et al., Tracking multiple components of a nuclear wavepacket in photoexcited Cu(I)-phenanthroline complex using ultrafast X-ray spectroscopy, *Nat. Commun.* 10 (2019) 3606. doi:10.1038/s41467-019-11499-w.
- [39] P. Wernet, K. Kunnus, I. Josefsson, I. Rajkovic, W. Quevedo, M. Beye, et al., Orbital-specific mapping of the ligand exchange dynamics of Fe(CO)₅ in solution, *Nature.* 520 (2015) 78–81. doi:10.1038/nature14296.

- [40] S. Eckert, J. Norell, P.S. Miedema, M. Beye, M. Fondell, W. Quevedo, et al., Ultrafast Independent N–H and N–C Bond Deformation Investigated with Resonant Inelastic X-Ray Scattering, *Angew. Chemie Int. Ed.* 56 (2017) 6088–6092. doi:10.1002/anie.201700239.
- [41] R.M. Jay, J. Norell, S. Eckert, M. Hantschmann, M. Beye, B. Kennedy, et al., Disentangling Transient Charge Density and Metal–Ligand Covalency in Photoexcited Ferricyanide with Femtosecond Resonant Inelastic Soft X-ray Scattering, *J. Phys. Chem. Lett.* 9 (2018) 3538–3543. doi:10.1021/acs.jpcclett.8b01429.
- [42] Y. Liu, T. Harlang, S.E. Canton, P. Chábera, K. Suárez-Alcántara, A. Fleckhaus, et al., Towards longer-lived metal-to-ligand charge transfer states of iron(ii) complexes: an N-heterocyclic carbene approach, *Chem. Commun.* 49 (2013) 6412. doi:10.1039/c3cc43833c.
- [43] Y. Liu, P. Persson, V. Sundström, K. Wärnmark, Fe *N*-Heterocyclic Carbene Complexes as Promising Photosensitizers, *Acc. Chem. Res.* 49 (2016) 1477–1485. doi:10.1021/acs.accounts.6b00186.
- [44] K.S. Kjær, N. Kaul, O. Prakash, P. Chábera, N.W. Rosemann, A. Honarfar, et al., Luminescence and reactivity of a charge-transfer excited iron complex with nanosecond lifetime, *Science* (80-.). 363 (2019) 249–253. doi:10.1126/science.aau7160.
- [45] T.C.B. Harlang, Y. Liu, O. Gordivska, L.A. Fredin, C.S. Ponceca, P. Huang, et al., Iron sensitizer converts light to electrons with 92% yield, *Nat. Chem.* 7 (2015) 883–889. doi:10.1038/nchem.2365.
- [46] L.A. Fredin, M. Pápai, E. Rozsályi, G. Vankó, K. Wärnmark, V. Sundström, et al., Exceptional Excited-State Lifetime of an Iron(II)–*N*-Heterocyclic Carbene Complex Explained, *J. Phys. Chem. Lett.* 5 (2014) 2066–2071. doi:10.1021/jz500829w.
- [47] M. Pápai, G. Vankó, T. Rozgonyi, T.J. Penfold, High-Efficiency Iron Photosensitizer Explained with Quantum Wavepacket Dynamics, *J. Phys. Chem. Lett.* 7 (2016) 2009–2014. doi:10.1021/acs.jpcclett.6b00711.
- [48] M. Pápai, T. Rozgonyi, T.J. Penfold, M.M. Nielsen, K.B. Møller, Simulation of ultrafast excited-state dynamics and elastic x-ray scattering by quantum wavepacket dynamics, *J. Chem. Phys.* 151 (2019) 104307. doi:10.1063/1.5115204.
- [49] D. Leshchev, T.C.B. Harlang, L.A. Fredin, D. Khakhulin, Y. Liu, E. Biasin, et al., Tracking the picosecond deactivation dynamics of a photoexcited iron carbene complex by time-resolved X-ray scattering, *Chem. Sci.* 9 (2018) 405–414. doi:10.1039/C7SC02815F.
- [50] H. Tatsuno, K.S. Kjaer, K. Kunnus, T. Harlang, C. Timm, M. Guo, et al., Hot branching dynamics in a light-harvesting iron carbene complex revealed by ultrafast x-ray emission spectroscopy, *Angew. Chemie Int. Ed.* (2019). doi:10.1002/anie.201908065.
- [51] T.K. Kim, J.H. Lee, M. Wulff, Q. Kong, H. Ihee, Spatiotemporal Kinetics in Solution Studied by Time-Resolved X-Ray Liquidography (Solution Scattering), *ChemPhysChem.* 10 (2009) 1958–1980. doi:10.1002/cphc.200900154.
- [52] K. Haldrup, M. Christensen, M. Meedom Nielsen, IUCr, Analysis of time-resolved X-ray scattering data from solution-state systems, *Acta Crystallogr. Sect. A Found. Crystallogr.* 66 (2010) 261–269. doi:10.1107/S0108767309054233.
- [53] K.S. Kjær, T.B. van Driel, J. Kehres, K. Haldrup, D. Khakhulin, K. Bechgaard, et al., Introducing a standard method for experimental determination of the solvent response in laser pump, X-ray probe time-resolved wide-angle X-ray scattering experiments on systems in solution, *Phys. Chem. Chem. Phys.* 15 (2013) 15003–15016. doi:10.1039/C3CP50751C.
- [54] I.H.M. van Stokkum, D.S. Larsen, R. van Grondelle, Global and target analysis of time-resolved spectra, *Biochim. Biophys. Acta - Bioenerg.* 1657 (2004) 82–104. doi:10.1016/J.BBABIO.2004.04.011.
- [55] A.O. Dohn, E. Biasin, K. Haldrup, M.M. Nielsen, N.E. Henriksen, K.B. Møller, et al., On the calculation of x-ray scattering signals from pairwise radial distribution functions, *J. Phys. B At. Mol. Opt. Phys.* 48 (2015) 244010. doi:10.1088/0953-4075/48/24/244010.
- [56] P. Chábera, L.A. Fredin, K.S. Kjær, N.W. Rosemann, L. Lindh, O. Prakash, et al., Band-selective dynamics in charge-transfer excited iron carbene complexes, *Faraday Discuss.* 216 (2019) 191–210. doi:10.1039/C8FD00232K.
- [57] M. Pápai, M. Abedi, G. Levi, E. Biasin, M.M. Nielsen, K.B. Møller, Theoretical Evidence of Solvent-Mediated Excited-State Dynamics in a Functionalized Iron Sensitizer, *J. Phys. Chem. C.* 123 (2019) 2056–2065. doi:10.1021/acs.jpcc.8b10768.
- [58] I. Bersuker, *The Jahn–Teller Effect*, Cambridge University Press, Cambridge, 2006. doi:10.1017/CBO9780511524769.
- [59] G. Peng, F.M.F. deGroot, K. Haemaelaenen, J.A. Moore, X. Wang, M.M. Grush, et al., High-resolution manganese x-ray fluorescence spectroscopy. Oxidation-state and spin-state

- sensitivity, *J. Am. Chem. Soc.* 116 (1994) 2914–2920. doi:10.1021/ja00086a024.
- [60] X. Wang, F.M.F. de Groot, S.P. Cramer, Spin-polarized x-ray emission of 3 d transition-metal ions: A comparison via K α and K β detection, *Phys. Rev. B.* 56 (1997) 4553–4564. doi:10.1103/PhysRevB.56.4553.
- [61] K. Siegbahn, C. Nordling, A. Fahlman, R. Nordberg, K. Hamrin, J. Hedman, et al., ESCA. Atomic, molecular and solid state structure studied by means of electron spectroscopy, Almqvist-Wiksells, Uppsala, 1967.
- [62] R.M. Jay, S. Eckert, M. Fondell, P.S. Miedema, J. Norell, A. Pietzsch, et al., The nature of frontier orbitals under systematic ligand exchange in (pseudo-)octahedral Fe(II) complexes, *Phys. Chem. Chem. Phys.* 20 (2018) 27745–27751. doi:10.1039/C8CP04341H.
- [63] M. Chollet, R. Alonso-Mori, M. Cammarata, D. Damiani, J. Defever, J.T. Delor, et al., The X-ray Pump–Probe instrument at the Linac Coherent Light Source, *J. Synchrotron Radiat.* 22 (2015) 503–507. doi:10.1107/S1600577515005135.
- [64] R. Alonso-Mori, J. Kern, D. Sokaras, T.-C. Weng, D. Nordlund, R. Tran, et al., A multi-crystal wavelength dispersive x-ray spectrometer., *Rev. Sci. Instrum.* 83 (2012) 073114. doi:10.1063/1.4737630.
- [65] H.T. Philipp, M.W. Tate, S.M. Gruner, Low-flux measurements with Cornell’s LCLS integrating pixel array detector, *J. Instrum.* 6 (2011) C11006. doi:10.1088/1748-0221/6/11/C11006.
- [66] M. Harmand, R. Coffee, M.R. Bionta, M. Chollet, D. French, D. Zhu, et al., Achieving few-femtosecond time-sorting at hard X-ray free-electron lasers, *Nat. Photonics.* 7 (2013) 215–218. doi:10.1038/nphoton.2013.11.
- [67] T.B. van Driel, K.S. Kjær, E. Biasin, K. Haldrup, H.T. Lemke, M.M. Nielsen, Disentangling detector data in XFEL studies of temporally resolved solution state chemistry, *Faraday Discuss.* 177 (2015) 443–465. doi:10.1039/C4FD00203B.
- [68] E. Biasin, T.B. van Driel, G. Levi, M.G. Laursen, A.O. Dohn, A. Moltke, et al., Anisotropy enhanced X-ray scattering from solvated transition metal complexes, *J. Synchrotron Radiat.* 25 (2018) 306–315. doi:10.1107/S1600577517016964.
- [69] I.F. Galván, M. Vacher, A. Alavi, C. Angeli, J. Autschbach, J.J. Bao, et al., OpenMolcas: From Source Code to Insight, (2019). doi:10.26434/chemrxiv.8234021.v1.
- [70] M.G. Delcey, L.K. Sørensen, M. Vacher, R.C. Couto, M. Lundberg, Efficient calculations of a large number of highly excited states for multiconfigurational wavefunctions, *J. Comput. Chem.* (2019) submitted.
- [71] P.Å. Malmqvist, A. Rendell, B.O. Roos, The restricted active space self-consistent-field method, implemented with a split graph unitary-group approach, *J. Phys. Chem.* 94 (1990) 5477–5482. doi:10.1021/j100377a011.
- [72] B.O. Roos, R. Lindh, P.A. Malmqvist, V. Veryazov, P.O. Widmark, Main group atoms and dimers studied with a new relativistic ANO basis set, *J. Phys. Chem. A.* 108 (2004) 2851–2858. doi:10.1021/jp031064+.
- [73] B.O. Roos, R. Lindh, P.Å. Malmqvist, V. Veryazov, P.O. Widmark, New relativistic ANO basis sets for transition metal atoms, *J. Phys. Chem. A.* 109 (2005) 6575–6579. doi:10.1021/jp0581126.
- [74] M. Douglas, N.M. Kroll, Quantum electrodynamical corrections to fine-structure of helium, *Ann. Phys.* 82 (1974) 89–155. doi:10.1016/0003-4916(74)90333-9.
- [75] B.A. Hess, Relativistic electronic-structure calculations employing a 2-component no-pair formalism with external-field projection operators, *Phys. Rev. A.* 33 (1986) 3742–3748. doi:10.1103/PhysRevA.33.3742.
- [76] P.Å. Malmqvist, B.O. Roos, B. Schimmelpfennig, The restricted active space (RAS) state interaction approach with spin-orbit coupling, *Chem. Phys. Lett.* 357 (2002) 230–240. doi:10.1016/s0009-2614(02)00498-0.
- [77] P.A. Malmqvist, K. Pierloot, A.R.M. Shahi, C.J. Cramer, L. Gagliardi, The restricted active space followed by second-order perturbation theory method: theory and application to the study of CuO₂ and Cu₂O₂ systems., *J. Chem. Phys.* 128 (2008) 204109. doi:10.1063/1.2920188.